




Multicentre investigation of neutron contamination at cardiac implantable electronic device (CIED) location due to high-energy photon beams using passive detectors and Monte Carlo simulations

A. Mele¹, H. Aslian³, M. Bolzonella^{1,a} , M. Caresana¹, R. Ciolini⁴, F. d'Errico^{4,5}, F. Longo^{2,6}, C. Mordacchini⁷, M. Quattrocchi⁸, S. Ren Kaiser⁹, D. Siqueira Nascimento⁴, M. Severgnini⁹, E. Tuttoilmondo¹

¹ Dipartimento di Energia, Politecnico di Milano, Via Lambruschini 4, 20156 Milan, Italy

² Dipartimento di Fisica, Università di Trieste, Via Alfonso Valerio, 2, 34127 Trieste, Italy

³ Department of Radiation Oncology, Olivia Newton-John Cancer Wellness & Research Center, Austin Hospital, 145 Studley Road, Heidelberg, VIC, Australia

⁴ Dipartimento di Ingegneria Civile e Industriale, Università di Pisa, Largo Lazzarino, 1, 56122 Pisa, Italy

⁵ School of Medicine, Yale University, 333 Cedar St, New Haven, CT 06510, USA

⁶ INFN, Sezione di Trieste, Via Alfonso Valerio, 2, 34127 Trieste, Italy

⁷ S. C. Fisica Sanitaria, ASST dei Sette Laghi, Viale Luigi Borri, 57, 21100 Varese, Italy

⁸ Azienda USL Toscana Nord Ovest, Lucca, Italy

⁹ Struttura di Fisica Sanitaria, Azienda Sanitaria Universitaria Giuliano-Isontina, Trieste, Italy

Received: 28 June 2023 / Accepted: 11 October 2023

© The Author(s) 2023

Abstract Radiotherapy treatments involving LINACs operating at accelerating potentials >10 MV generate (photo)neutrons which deliver dose to patients also outside the target volume. This effect is particularly relevant for patients with cardiac implantable electronic devices (CIEDs), which can be damaged by the therapeutic irradiation. In the last few years, there has been a rising interest in this issue, and it seems that damage to CIEDs is primarily associated with the thermal component of the photoneutron field. In particular, a recent study led by Politecnico di Milano considered CIEDs from various manufacturers and showed that some of these devices can be damaged after an irradiation with a thermal neutron fluence of about 10^9 cm⁻². The present work results from a collaboration among Politecnico di Milano, the University of Pisa, the University of Trieste and three Italian hospitals located in Lucca, Trieste and Varese, respectively, and it is primarily aimed at evaluating the thermal neutron fluence in CIED region for some high-energy treatments delivered at 15 MV and 18 MV and to determine whether it is comparable to the critical value given above, which has been experimentally determined to be potentially harmful for CIEDs. Thermal neutron fluence was measured through CR-39 detectors and TLDs, which were housed inside a BOMAB-like phantom mimicking the patient's trunk. The experimental sessions involved two models of LINAC, *Varian Clinac DHX* (Varese hospital) and *Elekta Synergy* (Lucca and Trieste hospitals). The experimental results show that the treatments considered in this study can lead to a thermal neutron fluence in the cardiac region comparable to the critical value. Furthermore, detailed Monte Carlo geometries for the facilities involved in this project were developed with the MCNP code (v. 6.2), and they were tested by comparing simulation results to measurements considering some benchmark irradiation plans. Bubble detectors were also employed for fast neutron fluence measurements to be compared to simulation outputs. These computational models stand out as promising tools for the investigations required in this work, and they can be used for further studies also extending their use to analogous facilities hosting the same models of LINACs.

1 Introduction

As the number of patients with cardiac implantable electronic devices (CIEDs) undergoing radiotherapy increases, it presents challenges for radiation oncologists, radiation therapists, cardiologists and medical physicists. The safety concerns and uncertainty surrounding the optimal treatment planning, patient monitoring and device interrogations during and/or after radiotherapy create challenges in managing these patients. Many of these challenges, however, have already been addressed in the literature as well as in national and international guidelines [1–5].

The AAPM-TG 203 [1] practice guidelines for managing patients with cardiac implantable electronic devices (CIEDs) during radiotherapy classify CIED patients into risk categories. These categories are determined not only by the cumulative dose to the CIED and patient pacing dependency but also by the presence of (photo)neutrons during the delivery of radiation therapy.

^a e-mail: matteo.bolzonella@polimi.it (corresponding author)

Table 1 Recommended experimental GDR parameters for selected LINAC nuclides (data referred to the total photoabsorption cross section)

Nuclide	Resonance energy (MeV)	FWHM (MeV)	σ_{\max} (mb)
Fe-54	19.35	5.50	147.00
Cu-63	16.43	4.84	79.79
	20.15	5.52	49.39
	19.62	8.09	86.38
W-182	11.98	3.91	283.99
	14.94	5.16	259.40
W-184	11.92	4.52	347.68
	15.05	3.87	233.17
W-186	13.04	6.60	410.29
	14.89	2.12	69.05
Pb-206	13.58	3.83	512.45
Pb-207	13.55	3.95	479.80
Pb-208	13.37	3.93	645.49

Data are taken from Table III of [8]. For nuclides with a GDR composed of two peaks, two lines of data are given

Photoneutrons are produced via (γ , xn) reactions between the primary photon beam and high-Z materials, including the main components in the LINAC head such as target, flattening filter, primary collimator, upper and lower jaws, and the head shielding. Neutrons are also produced in the patient's body and the structures in the treatment room such as walls, floor and ceiling. Neutron contamination can become significant for accelerating potentials above 10 MV [6]. The cross section accounting for all possible photonuclear reactions of nuclei (total photoabsorption cross section) typically shows a broad resonance in the energy region from ~ 10 to 25 MeV with the shape of a single or double peak known as giant dipole resonance (GDR). This resonance is connected to the collective oscillations of nucleons (protons vs neutrons), and it is also the main responsible for photoneutron production [7]. The GDR parameters for the LINAC nuclides which are the predominant source of photoneutron are given in Table 1 – note that for heavy nuclei photonuclear reactions basically mean photoneutron production [8]. A rich database of photonuclear data can be found in [8]. The energy spectrum of neutron fluence at the isocentre within the air typically exhibits two distinct peaks. The first, known as the fast peak, is centred at approximately 1 MeV and primarily comprises evaporation neutrons. The second peak, referred to as the thermal peak, is composed of neutrons that have been undergone thermalization. Photoneutrons are initially emitted as fast neutrons, while the thermal peak is generated through neutron moderation within the treatment room environment, predominantly in the air and walls. The dominance of the thermal component increases with distance from the isocentre, as fast and epithermal neutrons gradually lose energy through interactions with the surrounding medium, ultimately reaching thermal energies, as referenced in [9, 10]. A similar phenomenon is observed when the isocentre is positioned in a low-Z target, such as the patient's body or a phantom, where hydrogen prominently contributes to the reduction of neutron energy (as noted in [11]). It is noteworthy that at greater distances from the isocentre, the quantity of thermal neutrons in the treatment room remains relatively constant. This constancy arises because fast neutrons experience reflection from room surfaces, emerging with epithermal and thermal energies – a phenomenon known as the room-return effect [11, 12].

Several studies [13, 14] have investigated the photoneutron characteristics in high-energy photon beams.

Neutron contamination leads to the production of high-linear-energy-transfer (LET) secondary particles which can have adverse effects on the memory and microprocessor circuits of CIEDs. The incidence of soft errors in CMOS is typically associated with thermal neutrons, whereas latch-up events are more commonly associated with fast neutrons [1, 15, 16]. Nonetheless, it appears that malfunctions in CIEDs primarily stem from thermal neutrons, and this can be attributed to two principal factors: (1) their elevated fluence within the patient's body, encompassing the CIED vicinity, when compared to that of fast neutrons, and (2) their effective capture by isotopes such as boron-10 (B-10) and lithium-6 (Li-6), which are present in the components of CIEDs [17]. In fact, glass film made of boron silicate is used for protecting semiconductor surfaces, making these devices prove to thermal neutron-induced radiation damage [18].

Single event occurrences are stochastic in nature, with the probability of these events increasing as the flux of high-LET particles increases. Consequently, the probability of neutron-induced damage rises with increasing photon energy, leading to higher neutron fluences. For instance, at 18 MV the neutron fluence is roughly two and ten times higher than that at 15 MV and 10 MV, respectively [1, 16].

Different authors have focused on the causes and mechanisms of CIED malfunctions during neutron-producing radiotherapy treatments [1, 14–17, 19–22]. In particular, the studies by Mathew and Zecchin [14, 17] have proposed the secondary photoneutron field present in the treatment room as a potential cause of device damage even when the devices are not situated in close proximity to the treatment field.

The present study builds upon an important finding from collaborative research led by Politecnico di Milano [23]. In this research, a sample of 95 CIEDs underwent irradiation at the NEUTRA station of Paul Scherrer Institut (PSI) with a thermal neutron fluence of approximately 10^9 n/cm² [23, 24]. An evaluation of CIED performance was conducted before and after the irradiation, revealing

that a fair number of the test devices experienced damage, such as battery discharge, re-initialization, standby mode disruption and other soft errors.

Therefore, the main objective of this study is to assess the thermal neutron fluence $\Phi_{n,th}$ resulting from conventional radiotherapy treatments utilizing high-energy photons (15 and 18 MV treatments) in the region where CIEDs are typically implanted. This evaluation will be accomplished by means of a combination of measurements and Monte Carlo simulations. The aim is to determine whether the obtained thermal neutron fluence is comparable to the critical value mentioned above, for which it has been experimentally observed that damage to CIEDs may occur.

2 Materials and methods

All measurements of neutron fluence were taken at three radiation therapy centres: the ‘Ospedale di Circolo e Fondazione Macchi – Azienda Socio Sanitaria Territoriale (ASST) dei Sette Laghi’ hospital in Varese; the ‘San Luca – Azienda USL Toscana Nord Ovest’ hospital in Lucca; and the ‘Ospedale Maggiore – Azienda Sanitaria Universitaria Giuliano Isontina (ASUGI)’ hospital in Trieste. The Varese hospital houses a *Varian Clinac DHX* (Palo Alto, California) LINAC, while the accelerator used at the Lucca and Trieste hospitals is an *Elekta Synergy* (Crawley, United Kingdom) LINAC. The experimental set-up was carefully designed to replicate the conditions of actual therapy sessions using a BOMAB-like phantom. Passive detectors were strategically placed within the phantom to evaluate $\Phi_{n,th}$. The subsequent sections provide a comprehensive description of all the devices and methods employed throughout the experimental campaign.

2.1 Detection systems

2.1.1 Politecnico di Milano (PoliMi)

2.1.2 CR-39 detectors

Solid-state nuclear track detectors (SSNTDs) made of poly-allyl diglycol carbonate (PADC), commercially known as CR-39, coupled to thin layers of boron carbide (B_4C) converter, enriched to 99% in ^{10}B were used (Fig. 1). Hence, the detection of *thermal* neutrons is made possible via the $^{10}B(n, \alpha)^7Li$ reaction ($\sigma_{n,th} = 3840$ b).

Boron nuclei absorb neutrons and emit secondary high-LET charged particles (α and 7Li), which release energy within the sensitive volume of the CR-39. This breaks molecular bonds along the ions’ paths, resulting in ‘latent tracks’. To observe the tracks, a chemical treatment called *etching* is necessary to enlarge and fix them in the material. The etching used consisted in a bath in a 6.25 mol/L aqueous solution of sodium hydroxide (NaOH) at 97.3 ± 0.1 °C for 40 min. After that, the nuclear track densities are analysed using the *Politrack*[®] system [25].

To isolate only the thermal component of the neutron spectrum, the measurements were repeated, in one case covering the detectors with cadmium plates. The signal from thermal photoneutrons is then shielded out and can be subtracted from the total one (thermal + epithermal + fast) measured without Cd plates.

Accordingly, the mean track density due to thermal photoneutrons (TD_{th}) [cm^{-2}] is converted to the quantity of interest, *thermal neutron fluence* $\Phi_{n,th}$, using a conversion factor ($f_{c,CR-39}$ [$n\ trk^{-1}$]), after subtraction of the average background track density (TD_{BKG}):

$$\Phi_{n,th} = (TD_{th} - TD_{BKG}) \cdot f_{c,CR-39} \quad (1)$$

The conversion factor ($f_{c,CR-39}$) was estimated through detectors calibration at Politecnico di Milano using a thermal neutron source obtained by moderating AmBe ($\varphi_{th} = 492\ cm^{-2}\ s^{-1} \pm 6\%$, $k = 2$) inside a cylinder of polyethylene (ESTHER facility [26]). $f_{c,CR-39}$ varies according to different batches of CR-39 and to different CR-39 manufacturers. For this study, CR-39 s from two batches, one from *RTP* (Reinforced ThermoPlastics Company) and one from *TASL* (Track Analysis Systems Ltd), were used, and the calibration procedure yielded a calibration factor (f_c) of, respectively, $143 \pm 8\ n\ trk^{-1}$ ($k = 2$) and $130 \pm 7\ n\ trk^{-1}$ ($k = 2$).

The detection system used in this study showed a very high sensitivity to thermal neutrons (1 track per ~ 200 neutrons) attributed to the significant enrichment of ^{10}B in the converter. It enables the measurement of thermal fluences on the order of $10^4\ n\ cm^{-2}$.

2.1.3 TLDs

Pairs of $4\ ^7LiF:Mg,Ti$ (TLD700) and $4\ ^6LiF:Mg,Ti$ (TLD600) thermoluminescent detectors (TLDs) were utilized, as shown in Fig. 2. The former TLDs are enriched to a purity of 99.9% in Li-7 and serve the purpose of photons detection, while the latter TLDs are enriched in Li-6 to a purity of 95.6% and serve the dual purpose of detecting photons and neutrons via the $^6Li(n, \alpha)^3H$ reaction. It is noteworthy that the neutron absorption cross section of Li-7 is significantly lower in comparison with the cross section of the (n, α) reaction on Li-6, which are approximately $5 \cdot 10^{-2}$ b and 950 b at thermal energies, respectively. Additionally, the quantity of

Fig. 1 3D rendering of the detection system obtained using the software *SOLIDWORKS*. The SSNTD, on which the identification code is engraved, is coupled to the boron converter and, on the right image, is covered with two cadmium plates. Images are not to scale

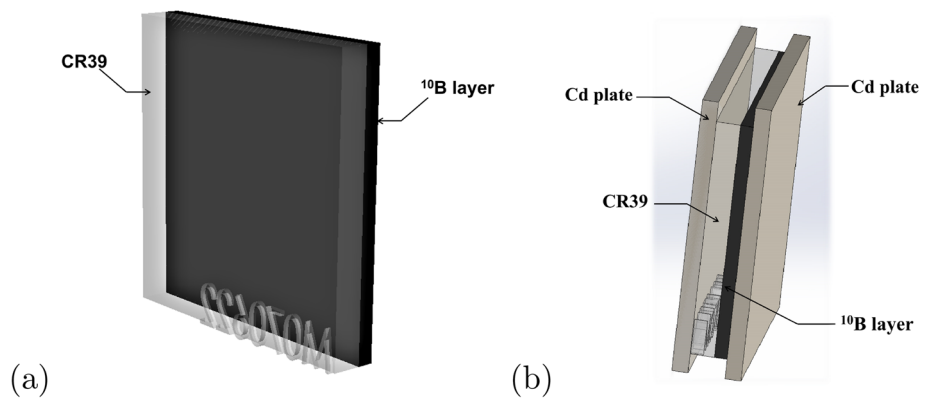
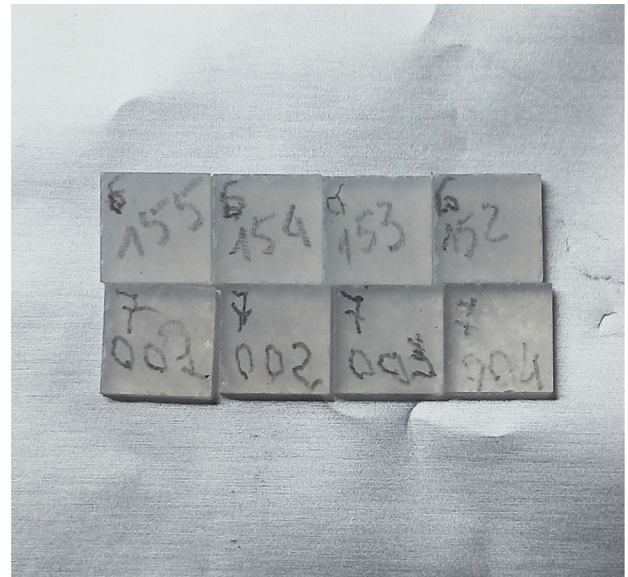


Fig. 2 Pairs of ${}^7\text{LiF:Mg,Ti}$ and ${}^6\text{LiF:Mg,Ti}$ TLDs. TLDs were wrapped in tinfoil to shield them from ambient light



Li-6 present in Li-7-enriched TLDs is minimal when contrasted with that in Li-6-enriched TLDs. Consequently, the neutron signal generated by Li-7-enriched TLDs is negligible in comparison with that of Li-6-enriched TLDs [27].

In this case, the thermal neutron fluence signal is obtained by subtracting the TLD700 signal (L_{700}) from the TLD600 one (L_{600}) and multiplying it by the conversion factor $f_{c,\text{TLD}}$ [$\text{cm}^{-2} \cdot \text{nC}^{-1}$]:

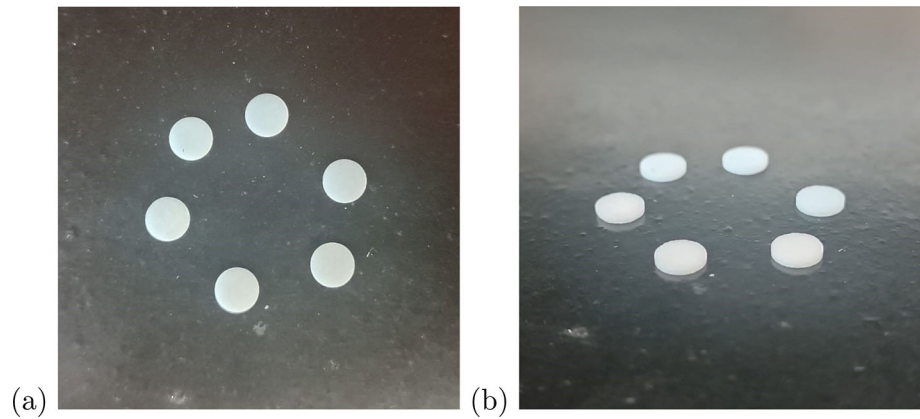
$$\Phi_{n,\text{th}} = (L_{600} - L_{700}) \cdot f_{c,\text{TLD}} \quad (2)$$

In doing so, each TLD reading was compensated by accounting for the corresponding sensitivity factor (i.e. a multiplicative factor leading to the average reading of the whole TLD set considered – the TLD600 set or the TLD700 one). For the TLD700 set, sensitivity factors were computed irradiating the crystals (placed behind a PMMA layer, to achieve charged particle equilibrium) with a reference ${}^{137}\text{Cs}$ source hosted at the Calibration Laboratory LAT n°104 of Politecnico di Milano, while for the TLD600 set these factors were evaluated irradiating the crystals in the $n+\gamma$ field of the moderated AmBe source of the ESTHER facility.

The conversion factor $f_{c,\text{TLD}}$ was calculated at the ESTHER facility, under the same conditions used for the CR-39s, and it is equal to $1.63 \cdot 10^6$ ($\text{cm}^{-2} \cdot \text{nC}^{-1}$) with a relative uncertainty of about 5% ($k = 2$). The TLD reader employed was a *Harshaw 5500* reader, with a thermal cycle consisting in a temperature ramp from 100 °C to 400 °C.

Also in this case, measurements were repeated shielding the instruments between Cd plates, to subtract the contribution from epithermal and fast neutrons. As the detectors have a sensitivity of about $1.6 \cdot 10^{-6}$ nC per unit of thermal neutron fluence but the reader used for the measurements has a minimum detectable signal of a few nC, the minimum detectable thermal fluence is of the order of 10^6 cm^{-2} .

Fig. 3 Pellets of GR-206A on the left and GR-207A on the right



2.1.4 Università di Pisa (UniPi)

2.1.5 TLDs

Thermoluminescent detectors used for the purpose of this study are in the form of crystals (Fig. 3). Due to the presence of neutron and gamma field, GR-206A and GR-207A sintered crystals (0.8 mm thick and 4.5 mm diameter) were selected, exploiting their high sensitivity and effective atomic number (8.2) very close to soft tissue. They are made of lithium fluoride doped with magnesium, copper and phosphorus (LiF:Mg,Cu,P) and are enriched with ^6Li and ^7Li , respectively. The light output of the GR-207A is determined by the gamma ray component alone, as the neutron contribution can be disregarded for the aforementioned reasons. In contrast, the signal from the GR-206A is attributable to both gamma rays and neutrons, with a predominant influence from low-energy neutrons primarily due to the I/ν behaviour exhibited by the $^6\text{Li}(n, \alpha)^3\text{H}$ cross section. For both crystals, the TL annealing cycle was performed at a temperature of 240° for a time of 35 min, and the readout step was divided in two steps: a preheating phase (20 s at 160°C) and an acquisition phase (20 s at 240°C). The reader was a *Harshaw mod.4500* TLD Workstation connected to a computer for data storing and processing.

To characterize the response to photon radiation, both TLD types (GR-206A and GR-207A) were firstly irradiated in packages coated with solid water (to ensure the charged particle equilibrium) with a calibrated ^{60}Co source (1.253 MeV, source uncertainty $\pm 6\%$, $k = 2$). The individual correction factor (sensitivity) of the crystals was determined with a dedicated gamma irradiation. Subsequently, to characterize the response to thermal neutron irradiation, the GR-206A and GR-207A crystals were irradiated at the ESTHER facility of Politecnico di Milano. Since the aim of this work is to measure the thermal neutron fluence, the following steps were performed:

- Determination of the thermal neutron conversion factor $F_{c,TLD}$ ($6.04 \cdot 10^3 \text{ cm}^{-2} \text{ nC}^{-1} \pm 2\%$, $k = 2$) through:

$$F_{c,TLD} = \frac{\Phi_{n,th,ref}}{L_{GR\ 206A} - L_{GR\ 207A}} \quad (3)$$

where $\Phi_{n,th,ref}$ is the reference thermal fluence [cm^{-2}], $L_{GR\ 206A}$ is the average reading [nC] of GR-206A crystals and $L_{GR\ 207A}$ is the average reading [nC] of GR-207A crystals.

- Determination of the thermal neutron fluence of the field through:

$$\Phi_{n,th} = \frac{(L_{GR\ 206A} - L_{GR\ 207A})}{MU} \cdot F_{c,TLD} \quad (4)$$

where $L_{GR\ 206A}$ and $L_{GR\ 207A}$ are the readings of GR-206A and GR-207A in the field and MU is the monitor unit relative to the exposure. The sensitivity factor of each crystal was considered in each calculation.

2.1.6 Bubble detectors

Finally, as anticipated in the introduction, bubble detectors for the measurement of fast neutron fluence were employed (Fig. 4). The detectors used in this study were superheated droplet (bubble) detectors manufactured in Yale University [28]. These detectors consist of a homogeneous dispersion of halocarbon droplets in a gel matrix. The halocarbon used was octafluorocyclobutane (C-318). They are contained in vials approximately 4.5 mL in volume, with an internal diameter of 14 mm and a height of 30 mm. Each detector contains 1.5 mL of active region, which consists of a neutron-sensitive emulsion with tens of thousands $60 \mu\text{m}$ droplets suspended in a glycerin-based gel, while the top of the detector is composed solely of inert gel.

To characterize the response to fast neutrons, bubble detectors were calibrated free in air with an AmBe neutron source ($6.7 \cdot 10^4 \text{ n/s}$ emission, source uncertainty $\pm 3\%$, $k = 2$). Subsequently, the number of bubbles generated in the detectors was quantified

Fig. 4 Bubble detectors before (a) and after (b) irradiation

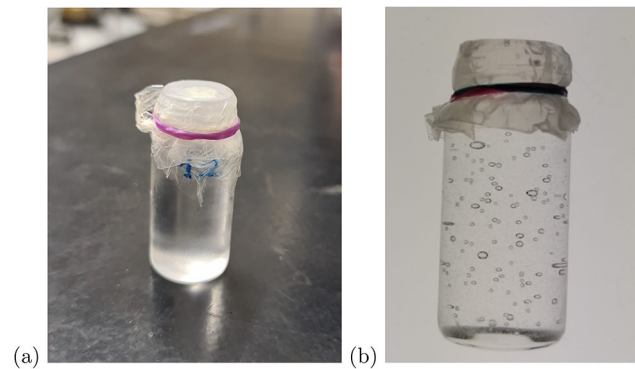
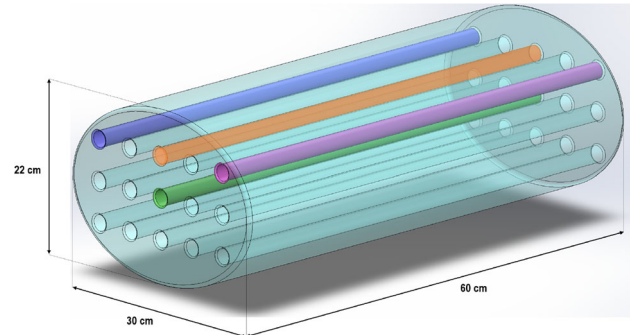


Fig. 5 3D rendering of the BOMAB-like phantom developed by the University of Pisa. The devices used in the experiments were positioned in channels 1 (blue), 3 (orange), 5 (purple) and 8 (green)



using the open-source software *ImageJ*, and a conversion factor $F_{BD} = 6.67 \cdot 10^3 \text{ cm}^{-2}/\text{bubble} \pm 20\%$ ($k = 2$), fast neutron fluence for bubble, was determined. The fast neutron fluence in the field was found through:

$$\Phi_{\text{fast neutrons}} = \frac{N_{\text{Field}} \cdot F_{BD}}{MU} \quad (5)$$

where N_{Field} is the number of bubbles counted in the field, F_{BD} is the conversion factor found in the calibration and MU is the monitor unit of the treatment.

2.2 BOMAB-like phantom

Throughout the experimental campaign, a BOMAB-like (BOMAB: BOTTle Manikin ABSorption) phantom was utilized (Fig. 5). This phantom, originally developed by the University of Pisa, is specifically designed to simulate the trunk of a patient.

The phantom used in the experimental study is an elliptic cylinder with walls constructed from polymethyl methacrylate (PMMA) that are 0.5 cm thick. It contains a 3×5 matrix of through PMMA pipes, each with a diameter of 2 cm and a wall thickness of 2 mm, arranged in a square lattice geometry. These pipes are designed to accommodate dosimeters or PMMA spacers. The phantom has dimensions of 60 cm in length, with the major and minor axes of the ellipse measuring 30 cm and 22 cm, respectively. The phantom consists of two bases, each 1 cm thick, which are made of polycarbonate. During the experiments conducted in Varese, the phantom was filled with water, while in Trieste and Lucca, it was filled with paraffin.

2.3 Irradiations

In Varese, the experimental set-up aimed to simulate an 18 MV treatment targeting a vertebra near the cardiac area. The irradiation field was set at $10 \times 10 \text{ cm}^2$, with the multileaf collimator (MLC) fully open. The isocentre was positioned 16 cm from the upper base of the phantom, centred horizontally. The treatment plan was repeated three times, gradually increasing the dose at the isocentre to validate the linearity of the response of the measuring devices. The detectors were placed in the upper left channel of the phantom (No. 1, marked in blue in Fig. 5), located 16 cm from the upper base of the phantom.

It is important to note that Cd plates were unavailable during these experiments, which prevented the measurement of the contribution associated with the epithermal component of the neutron spectrum and its subsequent subtraction from the total measurement. However, the obtained results remain significant for two primary reasons: first, the boron absorption cross section experiences a significant reduction in the range of epithermal energies following the $1/v$ law, resulting in decreased sensitivity of the device to epithermal neutrons; and second, the thermal component of the neutron spectrum dominates the epithermal component within the water phantom, as confirmed by MCNP simulations.

Table 2 Experimental results obtained using CR-39 detectors from Politecnico di Milano in terms of thermal neutron fluence per MU measured at CIED position

Hospital	Treatment area	Energy [MV]	MU delivered at isocentre	No. of detectors	$\Phi_{n,th} \left[\frac{1}{\text{cm}^2 \cdot \text{MU}} \right]$	Relative uncertainty (%)
Varese	Vertebra	18	20	8	$1.75 \cdot 10^5$	4
			40	4	$1.63 \cdot 10^5$	5
			100	4	$9.03 \cdot 10^4$ ^b	3
Trieste	Iliac wing	15	50 ^a	1	$6.24 \cdot 10^4$	3
Lucca	Iliac wing	15	50 ^a	2	$6.81 \cdot 10^4$	9

^a The total dose delivered to cadmium-shielded devices was 300 MU in Trieste and 200 MU in Lucca in order to obtain a measurable signal, which has been subtracted to the total one, once converted in $\text{cm}^{-2} \text{MU}^{-1}$

^b The neutron fluence is underestimated at the maximum dose value (100 MU) due to device saturation caused by high track density ($> 60\,000$ tracks/ cm^2). Therefore, this outlier value was excluded from further analyses

In Trieste and Lucca, the same 15 MV treatment plan targeting the iliac wing was simulated. The objective of these experiments was to investigate the thermal neutron fluence at the site of a CIED when the isocentre of a linear accelerator is located distally from the CIED implantation site. Therefore, the isocentre was placed 15 cm from the lower base of the phantom, horizontally centred. Detectors were arranged inside the upper right channel (No. 5, indicated in purple in Fig. 5) of the phantom, situated 13 cm from the upper base of the phantom.

Furthermore, in Trieste and Lucca, a 15 MV treatment with a fixed field size of $30 \times 30 \text{ cm}^2$ at the isocentre was used as a benchmark for the Monte Carlo (MC) models. Additional information regarding these tests can be found below.

3 Results and discussion

3.1 Experimental results

Tables 2 and 3 show the results of the measurements related to the CR-39 s and TLDs from PoliMi, respectively, while Table 4 presents the ones related to the TLDs from UniPi. They are expressed in terms of thermal neutron fluence ($\Phi_{n,th}$) per monitor unit (MU) delivered during the treatment ($100 \text{ MU} \simeq 1 \text{ Gy}$). Note that, to achieve a better statistics, some measurements were repeated, changing the detectors every time. Relative uncertainties reported in the tables correspond to one standard deviation (1σ).

3.1.1 Politecnico di Milano (PoliMi)

3.1.2 CR-39 detectors

To enhance the signal statistics, two separate detectors at a time were utilized by employing two CR-39s that faced a single ^{10}B converter in a sandwich configuration. However, this approach was not feasible for the measurements performed at the Trieste hospital because of the insufficient number of detectors available.

Results presented in Table 2 indicate a thermal neutron fluence of the order of $10^5 \text{ cm}^{-2} \text{ MU}^{-1}$ for a 15 MV treatment targeting a distal tumour with respect to the CIED (iliac wing). It is worth noting that there is a satisfactory agreement between the results obtained using *Elekta Synergy* accelerators of the same model but located in different facilities (Lucca and Trieste hospitals)

When treating an area adjacent to the CIED (vertebra) with higher-energy photon beams (18 MV), the neutron fluence significantly increases by about a factor of 2. To conclude, considering that typically a complete radiotherapy cycle requires doses ranging from 20 to 60 Gy, for the treatments analysed in this study, the measured thermal neutron fluence attains values comparable to the critical one reported in the introduction.

3.1.3 TLDs

For the vertebra treatment, the thermal neutron fluence is in the order of $10^5 \text{ cm}^{-2} \text{ MU}^{-1}$, consistent with the CR-39 data. The results for the iliac wing treatment delivered by LINACs of the same model at two different sites are comparable and similar to those of Table 2, but not as accurate as the CR-39 measurements, due to greater uncertainties resulting from the lower sensitivity of devices. Therefore, also in this case it is possible to conclude that values of thermal neutron fluence comparable to the critical one are achievable in a complete therapeutic cycle.

Table 3 Experimental results obtained using TLD dosimeters from Politecnico di Milano in terms of thermal neutron fluence per MU measured at CIED position

Hospital	Treatment area	Energy (MV)	MU delivered at isocentre	No. of detector pairs	$\Phi_{n,th} \left[\frac{1}{\text{cm}^2 \cdot \text{MU}} \right]$	Relative uncertainty (%)
Varese	Vertebra	18	20	20	$1.84 \cdot 10^5$	8
			40	12	$2.02 \cdot 10^5$	5
			100	8	$2.08 \cdot 10^5$	13
Trieste	Iliac wing	15	300 ^a	4	$7.40 \cdot 10^4$	5
Lucca	Iliac wing	15	300 ^a	4	$5.91 \cdot 10^4$	17

^aThe total dose delivered to cadmium-shielded devices was 500 MU in Trieste and 400 MU in Lucca in order to obtain a measurable signal. It has been subtracted to the total one, once converted in $\text{cm}^{-2} \text{MU}^{-1}$

Table 4 Experimental results obtained using TLD dosimeters from University of Pisa in terms of thermal neutron fluence per MU measured at CIED position

Hospital	Treatment area	Energy [MV]	MU delivered at isocentre	No. of detector pairs	$\Phi_{n,th} \left[\frac{1}{\text{cm}^2} \cdot \text{MU} \right]$	Relative uncertainty (%)
Varese	Vertebra	18	20	3	$2.76 \cdot 10^5$	17
			40	3	$1.59 \cdot 10^5$	30
Trieste	Iliac wing	15	500	3	$5.34 \cdot 10^4$	21
Lucca	Iliac wing	15	20	3	$7.96 \cdot 10^4$	41

3.1.4 Università di Pisa (UniPi)

3.1.5 TLD

The TLD UniPi measurements presented in Table 4 for both vertebra and iliac wing treatments demonstrated a response similar to the TLD PoliMi measurements presented in Table 3. Also, with this TLD type the results obtained for the iliac wing treatment at two different facilities using the same LINAC model were not accurate as those obtained from CR-39 measurements. One possible explanation for this inaccuracy could be the higher uncertainties associated with TLD UniPi measurements.

3.2 Monte Carlo simulations

In this study, two Monte Carlo models of an *Elekta Synergy* and *Varian Clinac DHX* accelerator heads were developed using the Monte Carlo N-particle extended code [29].

The *Elekta Synergy* model was initially modelled by the Trieste University group for studying photon and neutron out-of-field doses, fluence and energy spectra [16]. The Varian model, on the other hand, was developed by the PoliMi group exclusively for this research.

To construct a comprehensive representation of the set-up at the Trieste hospital, a 3D model of the LINAC head components (including bending magnets, flight tube, target, primary scatter filter, primary collimator, secondary flattening filter, ceramic ion chamber, backscatter plate, and diaphragm) as well as the LINAC bunker and BOMAB phantom were designed using AutoCAD software in SAT format. The SAT file was then converted into an MCNP input file using the MCNP visual editor (MCNPXVised, version 2.6). Material compositions and densities for each LINAC component were defined based on the manufacturer's documentation. Shielding materials for the LINAC head were selected from available literature, considering the similarity of materials typically used by manufacturers [16]. The initial parameters for the Gaussian energy spectrum, propagation direction and spot size of the electron beam striking the target were chosen based on estimated values provided by the manufacturer. The phantom was implemented directly in the MCNP input file by the PoliMi group.

The model of the Trieste facility was also extended to the Lucca facility being the LINAC model the same and the structure of the bunker similar.

As for the Varese hospital set-up, the LINAC model (head components and materials) was implemented using confidential documents by Varian Medical Systems dedicated to MCNP simulations of the Varian LINACs. A uniform disc of 18.3 MeV electrons, aligned in the vertical direction, was used as source term [30]. The bunker was built according to layout sketches from the Varese hospital.

Figure 6 presents some details of the geometrical model simulated with MCNP. To ensure accuracy and consistency of the developed models and their results, benchmark treatments were replicated through both simulations and experiments. The comparison between the thermal neutron fluence ($\Phi_{n,th}$) at a specific point in the phantom and the absorbed photon dose at the isocentre ($dose_{ph}$)

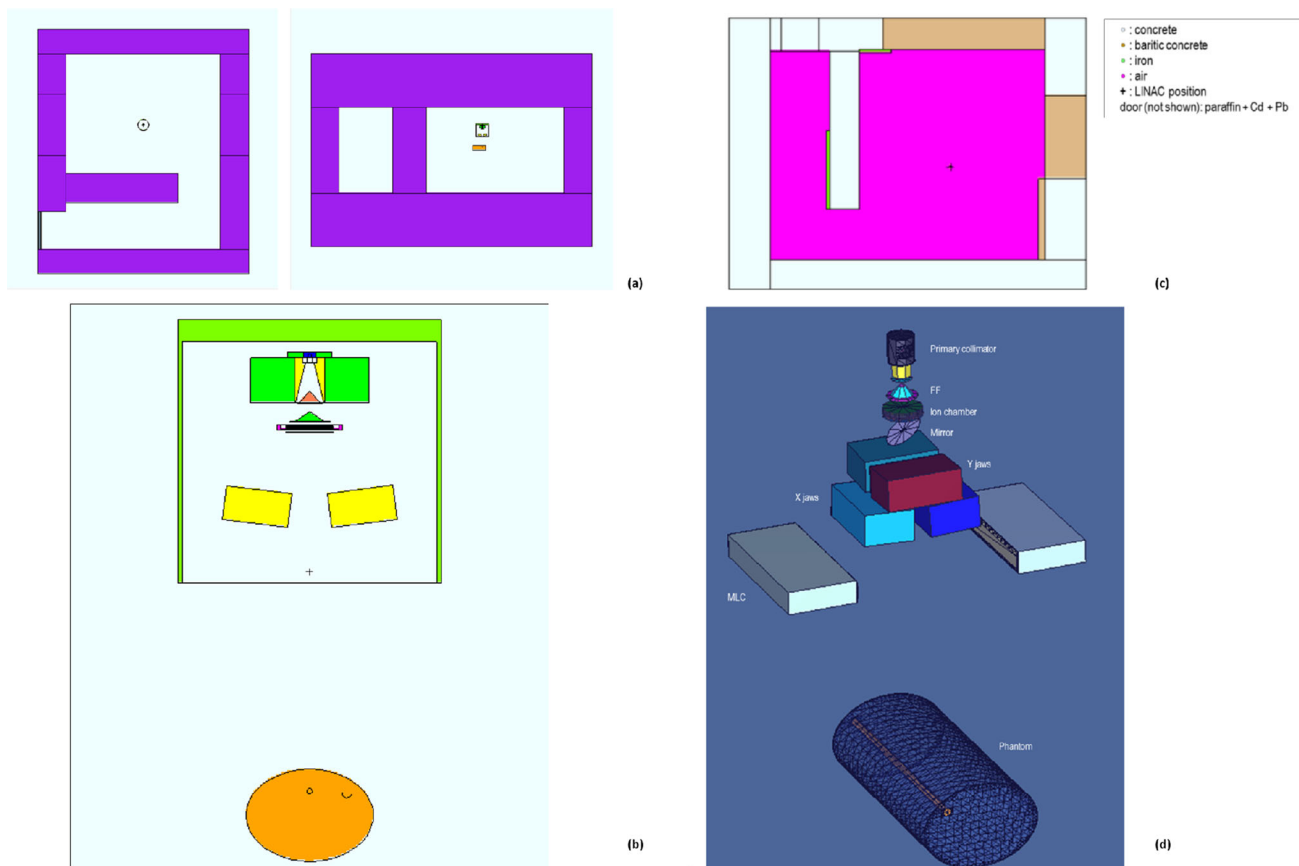


Fig. 6 On the left, 2D visualization of the Lucca and Trieste treatment room in the xy and xz planes (a) and the *Elekta Synergy* LINAC head components and phantom in the xz plane (b). On the right, xy view of Varese hospital bunker (c) and *Varian Clinac DHX* LINAC head components and phantom (d). Images acquired with the Visual Editor (*Vised v.22S*) associated with MCNP

was used as the basis for evaluation. $\Phi_{n,th}$ was obtained by integrating the neutron fluence calculated with tally F4:n within the energy bins corresponding to thermal energies. Tally volumes were cylindrical volumes of air with a radius equal to that of the phantom channels (1 cm) and a height of 3 cm (for the Trieste/Lucca model) or 5 cm (for the Varese model). The dose at the isocentre was calculated using tally F6:e within a spherical region of volume 1 cm^3 centred around the isocentre.

To achieve a better statistics for the results, variance reduction techniques were used: the BBREM card was used to enhance the production of photoneutrons, and the neutron importance was increased in the phantom and in the tally region.

As for the accuracy of the results, the most updated libraries available for the photon, neutron and electron cross sections were employed, as well as the cards needed for the correct thermal neutron scattering treatment in the light materials of interest (e.g. lwtr.20t for water).

During the experiments, $\Phi_{n,th}$ was measured by passive detectors, while the dose value was calculated by the Treatment Planning Systems.

The 18 MV treatment plan for the vertebra, previously described, was used to validate the model of the *Varian Clinac* in Varese. The irradiation layout is sketched in Figs. 7 and 8. The outcomes of simulations, which involved the use of $3 \cdot 10^8$ primary electrons, are shown in Table 5, compared to the results of experimental measurements. The last column is an indication of the distance between simulated and measured data.

The comparison between computed and measured data shows a good level of agreement, indicating that the model accurately reproduce the behaviour of the real system. The differences observed can be attributed to measurement errors and/or uncertainties in the model parameters. Overall, these results validate the use of the simulation model as a reliable tool for predicting the experimental results obtainable with CR-39 detectors or TLDs.

The computational model of the *Elekta Synergy* accelerator in Trieste and Lucca hospitals was tested using a 15 MV treatment with a fixed field size of $30 \times 30 \text{ cm}^2$ at the isocentre, centred at 15 cm from the bottom of the phantom, 4.5 cm deep from the surface and a source–surface distance (SSD) set to 100 cm. In this case, $9 \cdot 10^8$ primary particles were used. Figures 7 and 8 show the detectors set-up, while Tables 6, 7 and 8 compare the measured and simulated ratios for the various positions occupied by the detectors. It is important to underline that the measurement in position A' in Table 7 is affected by a $\sim 100\%$ uncertainty as the detector was positioned too close to the isocentre so that the photon signal hides completely the neutron one.

Fig. 7 PoliMi detectors arrangement during the measurements for validating the computational models and which was reproduced in MCNP simulations

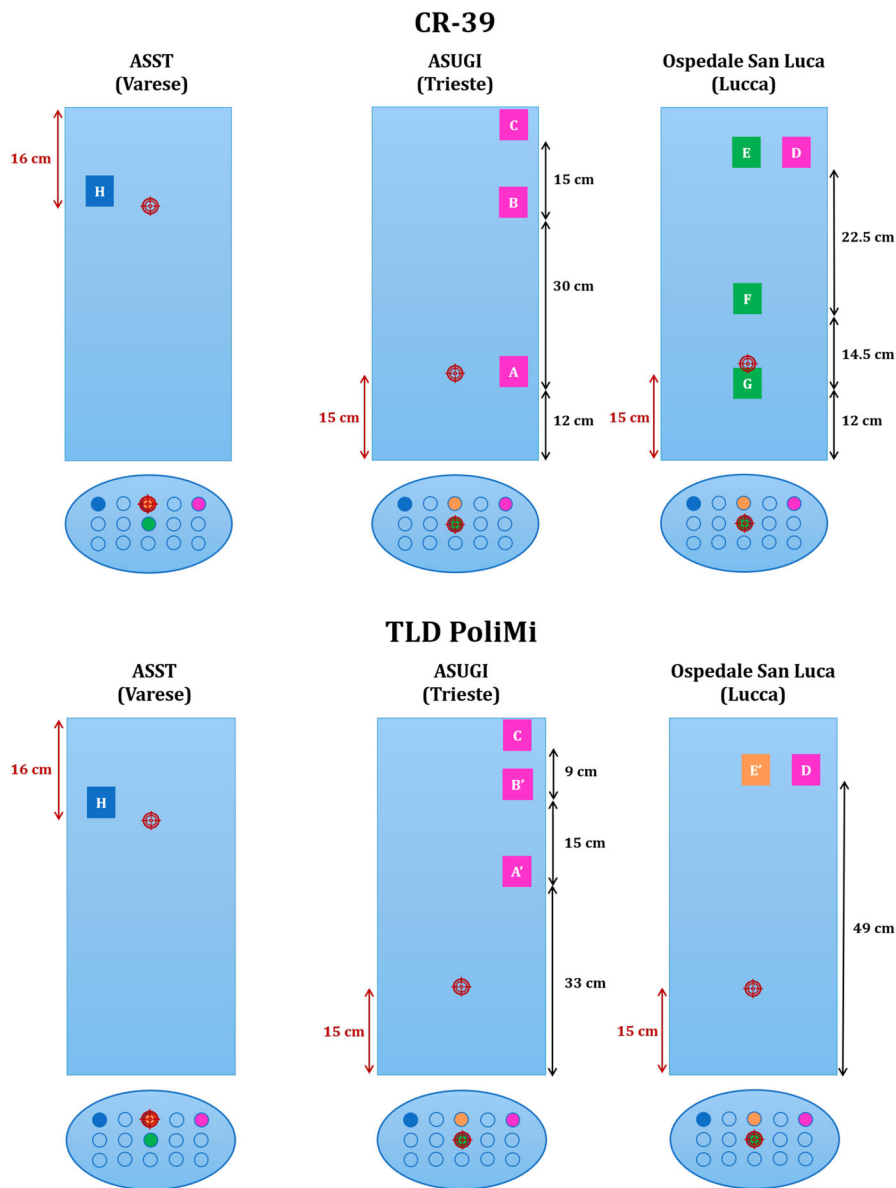


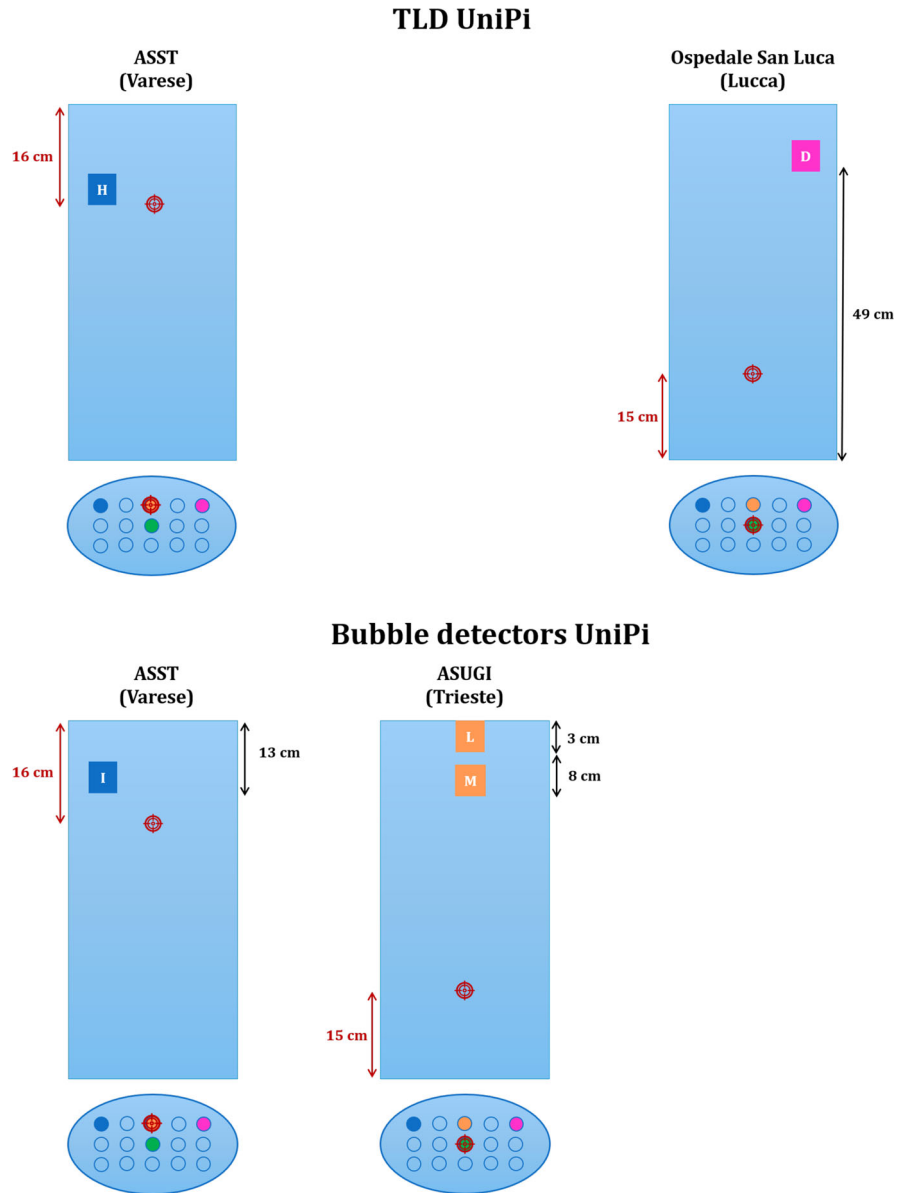
Table 5 Comparison between the results obtained by Monte Carlo simulations and through measurements at Varese hospital at CIED position (pos. H in Figs. 7 and 8)

	$\frac{\Phi_{n,th}}{dose_{ph}} \left[\frac{n}{cm^2 \cdot Gy} \right]$	Relative uncertainty (%)	Deviation % $\left[\frac{data_{MCNP} - data_{exp}}{data_{MCNP}} \right]$
MCNP 6.2	$1.62 \cdot 10^7$	8	–
CR-39	$1.69 \cdot 10^7$	3	– 4%
TLD PoliMi	$1.94 \cdot 10^7$	5	– 20%
TLD UniPi	$2.17 \cdot 10^7$	17	– 34%

In general, the MC code tends to overestimate the experimental results. Nevertheless, the agreement is reasonably good for the various positions considered, with the order of magnitude remaining always the same. Additionally, the code predicts the anticipated decreasing trend of the investigated quantity as one moves away from the isocentre.

In Fig. 9, the spectra of photoneutrons computed at various locations within the phantom are shown. Both spectra exhibit two main peaks: the first at thermal energies ($\sim 10^{-1}$ eV) and the second, relatively smaller, in the fast energy range ($\sim 10^6$ eV). This indicates that the thermal component of the neutron field within the patient’s body is dominant over the epithermal and fast components, deduction supported by experimental results obtained by bubble detectors (Table 9). Additionally, the simulation results confirm that this spectrum does not undergo significant changes when measured at different points along the main axis of the phantom, confirming the experimental measures, except for a minor increase at the isocentre. Note that the spectra related to the Lucca and

Fig. 8 UniPi detectors arrangement during the measurements for validating the computational models and which was reproduced in MCNP simulations



Trieste facilities refer to $9 \cdot 10^8$ primaries and the relative uncertainty (1σ) of the fluence values is about 2% in the thermal and epithermal region, while it is around 15% in the fast region; for the Varese facility, $3 \cdot 10^8$ primaries were employed, and the relative uncertainties (1σ) of the fluence values are about 3%, 5% and 30% for the thermal, epithermal and fast region, respectively.

3.2.1 Bubble detectors

The results presented in Table 9 indicate that the vertebra treatment resulted in a higher component of fast neutron fluence, with a magnitude of $10^4 \text{ cm}^{-2} \text{ MU}^{-1}$, compared to the iliac wing treatment, which showed magnitudes of 10^3 and $10^2 \text{ cm}^2 \text{ MU}^{-1}$ in two different positions. This difference in magnitude can be attributed to the different energy used, as it is well established that higher energy levels result in an increased photoneutron production. The results obtained from bubble measurements are consistent with the simulated spectra presented in Fig. 9, as they indicate a lower component of fast neutron fluence compared to thermal neutron fluence that was also obtained from CR-39 and TLDs dosimeters. Moreover, it can be noted that the fast neutron fluence decreases moving away from the isocentre, as predicted by the simulations.

Table 6 Comparison between the results obtained by Monte Carlo simulations and through measurements with CR-39 detectors at ASUGI (Trieste) and San Luca Hospital (Lucca)

Position	$\frac{\Phi_{n,th}^{exp}}{dose_{ph}^{exp}} \left[\frac{n}{cm^2 \cdot Gy} \right]$	Relative uncertainty (%)	$\frac{\Phi_{n,th}^{MCNP}}{dose_{ph}^{MCNP}} \left[\frac{n}{cm^2 \cdot Gy} \right]$	Relative uncertainty (%)	Deviation % $\left[\frac{data_{MCNP} - data_{exp}}{data_{MCNP}} \right]$
A	$3.84 \cdot 10^6$	3	$9.98 \cdot 10^6$	2	62%
B	$1.27 \cdot 10^6$	3	$5.05 \cdot 10^6$	3	75%
C	$1.60 \cdot 10^6$	3	$1.97 \cdot 10^6$	3	19%
D	$1.07 \cdot 10^6$	5	$4.25 \cdot 10^6$	3	75%
E	$2.26 \cdot 10^6$	4	$3.03 \cdot 10^6$	2	32%
F	$5.03 \cdot 10^6$	3	$5.97 \cdot 10^6$	2	16%
G	$6.35 \cdot 10^6$	3	$8.29 \cdot 10^6$	2	23%

Table 7 Comparison between the results obtained by Monte Carlo simulations and through measurements with TLD detectors from PoliMi at ASUGI (Trieste) and San Luca Hospital (Lucca)

Position	$\frac{\Phi_{n,th}^{exp}}{dose_{ph}^{exp}} \left[\frac{n}{cm^2 \cdot Gy} \right]$	Relative uncertainty (%)	$\frac{\Phi_{n,th}^{MCNP}}{dose_{ph}^{MCNP}} \left[\frac{n}{cm^2 \cdot Gy} \right]$	Relative uncertainty (%)	Deviation % $\left[\frac{data_{MCNP} - data_{exp}}{data_{MCNP}} \right]$
A'	$2.23 \cdot 10^6$	~ 100	$6.57 \cdot 10^6$	3	66%
B'	$2.18 \cdot 10^6$	42	$4.47 \cdot 10^6$	3	50%
C	$1.25 \cdot 10^6$	15	$1.97 \cdot 10^6$	3	36%
D	$1.17 \cdot 10^6$	30	$4.25 \cdot 10^6$	3	72%
E'	$2.70 \cdot 10^6$	18	$6.46 \cdot 10^6$	3	58%

Table 8 Comparison between the results obtained by Monte Carlo simulations and through measurements with TLD from UniPi at San Luca Hospital (Lucca)

Position	$\frac{\Phi_{n,th}^{exp}}{dose_{ph}^{exp}} \left[\frac{n}{cm^2 \cdot Gy} \right]$	Relative uncertainty	$\frac{\Phi_{n,th}^{MCNP}}{dose_{ph}^{MCNP}} \left[\frac{n}{cm^2 \cdot Gy} \right]$	Relative uncertainty	Deviation % $\left[\frac{data_{MCNP} - data_{exp}}{data_{MCNP}} \right]$
D	$2.74 \cdot 10^6$	30%	$4.25 \cdot 10^6$	6%	36%

Table 9 Experimental results obtained using bubble detectors in terms of fast neutron fluence per MU measured

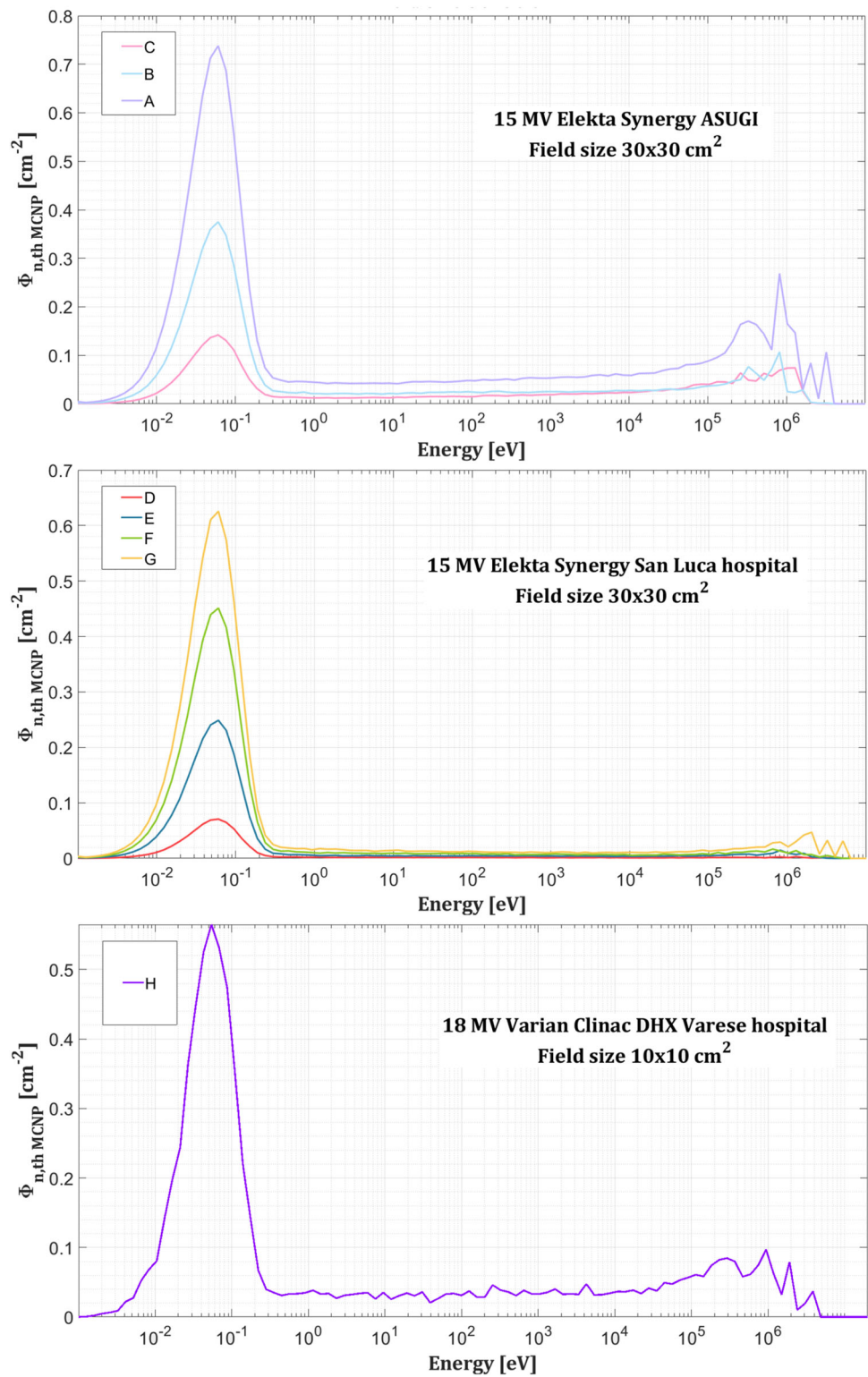
Position	Hospital	Treatment area	Energy (MV)	MU delivered at isocentre	No. of detectors	$\frac{\Phi_{n,f}}{MU} \left[\frac{1}{cm^2 \cdot MU} \right]$	Relative uncertainty
I	Varese	Vertebra	18	20	3	$2.84 \cdot 10^4$	40%
L	Trieste	Benchmark treatment	15	100	1	$2.69 \cdot 10^3$	16%
M		(fixed field $30 \times 30 \text{ cm}^2$)			1	$5.00 \cdot 10^2$	29%

4 Conclusions and perspectives

High-energy radiation therapy treatments can pose a risk to patients wearing a cardiac implantable electronic device. The major problem seems to be linked to the thermal component of the secondary photoneutron field generated in the treatment room, which can interfere with such devices leading to temporary or permanent malfunctions.

Therefore, the present work aims at characterizing this field, examining the area around the heart where a CIED is implanted. The measured value of thermal neutron fluence in this area was compared to the critical value for which malfunctions (soft errors) were experimentally observed to possibly occur, which is approximately $10^9 \frac{n}{cm^2}$ [23]. Passive detectors such as CR-39 SSNTDs coupled to ^{10}B converters and TLDs pairs were used to measure the quantity of interest inside a phantom that mimicked the human trunk, during simulated realistic treatment plans delivered at 15 MV and 18 MV. The results showed that the measured value was of the order of $10^5 \frac{n}{cm^2 \cdot MU}$. Hence, it is comparable to the critical value previously mentioned, assuming a complete course of conventional

Fig. 9 Photoneutrons spectra simulated using MCNP at different locations inside the phantom



radiotherapy (i.e., neither hypofractionated nor stereotactic therapy) where a patient receives a total dose of about 20 Gy to 60 Gy ($\sim 2 \cdot 10^3 - 6 \cdot 10^3$ MU). This result shall warn against possible damage to the CIEDs when such treatments are delivered, and further motivate research in this area, even if it must be noted that high-energy radiotherapy treatments are being progressively abandoned (especially the 18 MV ones). The present study paves the way to further investigations involving different, more complex treatment plans and accelerator models, and to studies of possible strategies to reduce the thermal neutron fluence on the devices (e.g. Cd shielding).

In any case, it is essential to better analyse and understand the damage to CIEDs as a function of the neutron fluence to be able to properly determine the level of risk posed by the secondary photon-neutron field.

Additionally, computational models have been developed and tested using experimental measurements. The MCNP 6.2 code was used to recreate the geometries of the accelerator heads, the phantom and the facility bunkers. The obtained results from the simulations are encouraging, as they accurately describe the radiation transport problem, and these models proved to be a promising tool to expand the study to other situations related to similar facilities. As a future development in this direction, the computational models could be improved by replacing the phantom model with a more realistic anthropomorphic voxel phantom and utilizing it to simulate actual treatment plans.

Funding Open access funding provided by Politecnico di Milano within the CRUI-CARE Agreement.

Data Availability Statement This manuscript has associated data in a data repository. [Authors' comment: The data that support the findings of this study are either included in this paper or available from the references. Further data about the experiments and simulations described in this work are available from the authors upon reasonable request.]

Declarations

Conflict of interest The authors declare that they have no known competing financial interests or personal relationships that could have appeared to influence the work reported in this paper.

Open Access This article is licensed under a Creative Commons Attribution 4.0 International License, which permits use, sharing, adaptation, distribution and reproduction in any medium or format, as long as you give appropriate credit to the original author(s) and the source, provide a link to the Creative Commons licence, and indicate if changes were made. The images or other third party material in this article are included in the article's Creative Commons licence, unless indicated otherwise in a credit line to the material. If material is not included in the article's Creative Commons licence and your intended use is not permitted by statutory regulation or exceeds the permitted use, you will need to obtain permission directly from the copyright holder. To view a copy of this licence, visit <http://creativecommons.org/licenses/by/4.0/>.

References

1. M. Miften, D. Mihailidis, S.F. Kry, C. Reft, C. Esquivel, J. Farr, D. Followill, C. Hurkmans, A. Liu, O. Gayou, M. Gossman, M. Mahesh, R. Popple, J. Prisciandaro, J. Wilkinson, Management of radiotherapy patients with implanted cardiac pacemakers and defibrillators: A report of the AAPM TG-203[†]. *Med. Phys.* **46**(12), 757–788 (2019). <https://doi.org/10.1002/mp.13838>
2. 2017 HRS Expert Consensus Statement on Cardiovascular Implantable Electronic Device Lead Management and Extraction—Heart Rhythm Society. Accessed 27 Feb 2023. <https://www.hrsonline.org/guidance/clinical-resources/2017-hrs-expert-consensus-statement-cardiovascular-implantable-electronic-device-lead-management>
3. B. Gauter-Fleckenstein, C. Barthel, S. Büttner, F. Wenz, M. Borggreffe, E. Tülümen, Effectivity and applicability of the German DEGRO/DGK-guideline for radiotherapy in CIED-bearing patients. *Radiother. Oncol.* **152**, 208–215 (2020). <https://doi.org/10.1016/j.radonc.2020.01.006>
4. M. Zecchin et al., Management of patients with cardiac implantable electronic devices (CIED) undergoing radiotherapy: a consensus document from Associazione Italiana Aritmologia e Cardioritmo (AIAC), Associazione Italiana Radioterapia Oncologica (AIRO), Associazione Italiana Fisica Medica (AIFM). *Int. J. Cardiol.* **255**, 175–183 (2018). <https://doi.org/10.1016/j.ijcard.2017.12.061>
5. A. Naseri, A. Mesbahi, A review on photoneutrons characteristics in radiation therapy with high-energy photon beams. *Rep. Pract. Oncol. Radiother.* **15**, 138–144 (2010). <https://doi.org/10.1016/j.rpor.2010.08.003>
6. M. Severgnini, L. Menegotti, A. Delana, T. Malatesta, M. Quattrocchi, H. Aslian, F. Pietrobon, S. Andreoli, F. Cattani, S.R. Kaiser, M. Eugenia, C. Foti, M.D. Falco, F. Guerriero, S. Recanello, A. Valentini, M. Stasi, [OA177] Contribution of the medical physicist to the Italian consensus document on management of patients with cardiac implantable devices (CIED) undergoing radiotherapy and future development from aifm working group. *Phys. Med.* **52**, 68 (2018). <https://doi.org/10.1016/j.ejmp.2018.06.249>. (Abstracts from the 2nd European Congress of Medical Physics)
7. B.M. Spicer, in *The Giant Dipole Resonance*. ed. by M. Baranger, E. Vogt (Springer, New York, 1969), pp. 1–78. https://doi.org/10.1007/978-1-4684-8343-7_1
8. T. Kawano, Iaea photonuclear data library 2019. *Nucl. Data Sheets* **163**, 109–162 (2020). <https://doi.org/10.1016/j.nds.2019.12.002>
9. A. Alem-Bezoubiri, F. Bezoubiri, A. Badreddine, H. Mazrou, Z. Lounis-Mokrani, Monte Carlo estimation of photoneutrons spectra and dose equivalent around an 18 MV medical linear accelerator. *Radiat. Phys. Chem.* **97**, 381–392 (2014). <https://doi.org/10.1016/j.radphyschem.2013.07.013>
10. A. Naseri, A. Mesbahi, A review on photoneutrons characteristics in radiation therapy with high-energy photon beams. *Rep. Pract. Oncol. Radiother.* **15**(5), 138–144 (2010). <https://doi.org/10.1016/j.rpor.2010.08.003>
11. H. Vega-Carrillo, A. Baltazar-Raigosa, Photoneutron spectra around an 18 MV LINAC. *J. Radioanal. Nucl. Chem. J. Radioanal. Nucl. Chem.* **287**, 323–327 (2011). <https://doi.org/10.1007/s10967-010-0696-0>
12. E.M.-A.E.L.A.B.R.M.-M.A.G.-V.J.L. Vega-Carrillo, H. R. Gallego, Neutron room return effect. *Revista Mexicana de Física*, 63–66 (2008)
13. R. Kaderka, D. Schardt, M. Durante, T. Berger, U. Ramm, J. Licher, C.L. Tessa, Out-of-field dose measurements in a water phantom using different radiotherapy modalities. *Phys. Med.* **57**(16), 5059 (2012). <https://doi.org/10.1088/0031-9155/57/16/5059>
14. F. Mathew, G.A. Makdassi, L. Montgomery, M. Evans, J. Kildea, The impact of treatment parameter variation on secondary neutron spectra in high-energy electron beam radiotherapy. *Phys. Med.* **80**, 125–133 (2020). <https://doi.org/10.1016/j.ejmp.2020.10.016>
15. B. Gauter-Fleckenstein, J. Nguyen, L. Jahnke, T. Gaiser, B. Rudic, S. Büttner, F. Wenz, M. Borggreffe, E. Tülümen, Interaction between CIEDs and modern radiotherapy techniques: Flattening filter free-VMAT, dose-rate effects, scatter radiation, and neutron-generating energies. *Radiother. Oncol.* **152**, 196–202 (2020). <https://doi.org/10.1016/j.radonc.2019.12.007>
16. H. Aslian, M. Severgnini, N. Khaledi, S. Ren Kaiser, A. Delana, R. Vidimari, M. de Denaro, F. Longo, Neutron and photon out-of-field doses at cardiac implantable electronic device (CIED) depths. *Appl. Radiat. Isot.* **176**, 109895 (2021). <https://doi.org/10.1016/j.apradiso.2021.109895>
17. M. Zecchin et al., Malfunction of cardiac devices after radiotherapy without direct exposure to ionizing radiation: mechanisms and experimental data. *Europace* **18**, 288–293 (2016). <https://doi.org/10.1093/europace/euv250>

18. U. Hansen, S. Maus, J. Leib, M. Töpper, Robust and hermetic borosilicate glass coatings by e-beam evaporation. *Procedia Chem.* **1**(1), 76–79 (2009). <https://doi.org/10.1016/j.proche.2009.07.019>. (Proceedings of the Eurosensors XXIII conference)
19. H. Aslian, T. Kron, T. Watts, C. Akalanli, N. Hardcastle, P. Lonski, A. Montaseri, B. Hay, J. Korte, K. Berk, F. Longo, M. Severgnini, The effect of stereotactic body radiotherapy (SBRT) using flattening filter-free beams on cardiac implantable electronic devices (CIEDs) in clinical situations. *J. Appl. Clin. Med. Phys.* **21**(6), 121–131 (2020). <https://doi.org/10.1002/acm2.12873>
20. R. Kakino, M. Nakamura, N. Hu, H. Iramina, H. Tanaka, Y. Sakurai, T. Mizowaki, Photoneutron-induced damage reduction for cardiac implantable electronic devices using neutron-shielding sheets in high-energy X-ray radiotherapy: a phantom study. *Phys. Med.* **89**, 151–159 (2021). <https://doi.org/10.1016/j.ejmp.2021.07.036>
21. A.O. Ezzati, M.T. Studenski, Design of a neutron applicator to reduce damage in cardiac implantable electronic devices. *Eur. Phys. J. Plus* **134**(8), 406 (2019). <https://doi.org/10.1140/epjp/i2019-12851-3>
22. A.O. Ezzati, M.T. Studenski, Neutron damage induced in cardiovascular implantable electronic devices from a clinical 18 MV photon beam: a Monte Carlo study. *Med. Phys.* **44**(11), 5660–5666 (2017)
23. C. Ferrante, Study of neutron-induced damage to cardiac implantable electronic devices in radiation therapy. Master's thesis, Politecnico di Milano (A.A. 2019-2020). Chap. 4. <http://hdl.handle.net/10589/175497>
24. E.H. Lehmann, P. Vontobel, L. Wiezel, Properties of the radiography facility NEUTRA ar SINQ and its potential for use as European reference facility. *Nondestr. Test. Eval.* **16**(2–6), 191–202 (2001). <https://doi.org/10.1080/10589750108953075>
25. M. Caresana, M. Ferrarini, A. Parravicini, Analisi Morfologica delle Tracce nucleari sui rivelatori CR-39. (6 June 2008). AIRP—Atti del Convegno Nazionale di Radioprotezione “Cinquantenario AIRP: Storia e Prospettive della Radioprotezione”
26. A. Bassanetti, Sviluppo di uno spettrometro direzionale per la misura della componente neutronica della radiazione cosmica. Master's thesis, Politecnico di Milano (A.A. 2015-2016)
27. E. Bezak, R. Takam, L.G. Marcu, Peripheral photon and neutron doses from prostate cancer external beam irradiation. *Radiat. Prot. Dosim.* **167**(4), 591–601 (2015). <https://doi.org/10.1093/rpd/ncu362>
28. F. d'Errico, Radiation dosimetry and spectrometry with superheated emulsions. *Nucl. Instrum. Methods Phys. Res. Sect. B Beam Interact. Mater. Atoms* **184**(1), 229–254 (2001). [https://doi.org/10.1016/S0168-583X\(01\)00730-3](https://doi.org/10.1016/S0168-583X(01)00730-3)Dosimetry. (**Advanced Topics in Solid State**)
29. C.J. Werner et al., MCNP Users Manual—Code Version 6.2, (2017). Los Alamos National Security, LLC
30. D. Sheikh-Bagheri, D.W. Rogers, Monte Carlo calculation of nine megavoltage photon beam spectra using the beam code. *Med. Phys.* **29**(3), 391–402 (2002). <https://doi.org/10.1118/1.1445413>